

### Numerical Heat Transfer, Part A: Applications



ISSN: 1040-7782 (Print) 1521-0634 (Online) Journal homepage: http://www.tandfonline.com/loi/unht20

# BUOYANCY-INDUCED HEAT TRANSFER IN PARTIALLY DIVIDED TRAPEZOIDAL CAVITIES

F. Moukalled & S. Acharya

To cite this article: F. Moukalled & S. Acharya (1997) BUOYANCY-INDUCED HEAT TRANSFER IN PARTIALLY DIVIDED TRAPEZOIDAL CAVITIES, Numerical Heat Transfer, Part A: Applications, 32:8, 787-810, DOI: 10.1080/10407789708913918

To link to this article: <a href="http://dx.doi.org/10.1080/10407789708913918">http://dx.doi.org/10.1080/10407789708913918</a>



Full Terms & Conditions of access and use can be found at http://www.tandfonline.com/action/journalInformation?journalCode=unht20

## BUOYANCY-INDUCED HEAT TRANSFER IN PARTIALLY DIVIDED TRAPEZOIDAL CAVITIES

#### F. Moukalled

Department of Mechanical Engineering, Faculty of Engineering and Architecture, American University of Beirut, Beirut, Lebanon

#### S. Acharya

Mechanical Engineering Department, Louisiana State University, Baton Rouge, Louisiana, USA

Numerical results are reported for natural convection heat transfer in partially divided trapezoidal cavities representing attic spaces. Two boundary conditions are considered. In the first, corresponding to summer-like conditions, the vertical and upper surfaces are heated while the lower surface is cooled. In the second, corresponding to winter-like conditions, the lower surface is heated while the other surfaces are cooled. The effects of Rayleigh number, baffle height, and baffle location on the heat transfer are investigated. Results are displayed in terms of streamlines, isotherms, velocity and temperature profiles, and local and average Nusselt number values. In winter-like conditions, convection starts to dominate at a Rayleigh number much lower than that in summer-like conditions. For both boundary conditions, the presence of baffles decreases heat transfer. For the bottom-cooled case this decrease is greater with a taller baffle, placed closer to the heated walls. For the bottom-heated case the decrease in heat transfer due to the baffles is greater with increasing distance from the vertical wall. Average Nusselt number correlations for both boundary conditions are presented.

#### **INTRODUCTION**

Buoyancy-induced heat transfer in rectangular enclosures and cylindrical annuli has been extensively studied in the literature. Ostrach [1] has recently presented a comprehensive review of the work done in this area. Comparatively little attention has been given, however, to natural convection heat transfer in enclosures of more complex geometry. Studies on natural convection in trapezoidal cavities have been very limited and have dealt only with the no-baffle situations where the convective motion of the fluid filling the enclosure was unimpeded. In this article, natural convection in partially divided trapezoidal enclosures is investi-

Received 14 May 1996; accepted 22 July 1997.

The financial support provided by the University Research Board of the American University of Beirut through Grant No. 48720 is gratefully acknowledged. Computations were performed in the Department of Mechanical and Mechatronic Engineering at the University of Sydney, Sydney, Australia. Special thanks are due to Professor M. Masri for allowing the use of his computational facilities and to Professor D. Fletcher for performing the FLOW-3D computations.

Address correspondence to Professor Sumanta Acharya, Department of Mechanical Engineering, Louisiana State University, Baton Rouge, LA 70803-6413, USA.

	NOMENO	CLATURE	
a	coefficients in the finite difference equation	<i>x</i> , <i>X</i>	dimensional and dimensionless coordinate along the horizontal
b c <sub>p</sub> e, E	local imbalance of mass specific heat of fluid east face of a control volume; east neighbor of the P grid point	<i>y</i> , <i>Y</i>	direction dimensional and dimensionless coordinate along the vertical direction
$G_1,G_2$	gravitational acceleration convective terms normal to grid cell	$\alpha, \beta, \gamma$	metric quantity; $\beta$ is also coefficient of thermal expansion
$h, \overline{h}$	boundaries local and average convection heat	$\Gamma^{\Phi}$ δ $\xi$ , δ $\eta$	diffusion coefficient distance between grid points
Н	transfer coefficient height of cavity at baffle midpoint	$\Delta \xi, \Delta \eta$	in $\xi$ and $\eta$ directions control volume spacing in $\xi$ and $\eta$
Ĥ J	height of the vertical side wall Jacobian	$\theta$ , $\theta$ <sub>b</sub>	directions dimensionless temperature;
$k, k_{\rm b}, k_{\rm r}$	thermal conductivity; baffle thermal conductivity; dimensionless baffle	ν	dimensionless baffle temperature kinematic viscoity
n, N	conductivity north face of a control volume; north	ξ, η ρ	transformed coordinate density
Nu, Nu*	neighbor of the P grid point local and normalized Nusselt number	Φ <i>ψ</i>	dependent variable stream function
$\overline{N}u, \overline{N}u^*$	average and normalized average Nusselt number	·	
p, P	thermodynamic pressure; dimensionless pressure;	Subscripts	
Pr	also main grid point	С	cold wall
Ra	Prandtl number $(= \mu c_p k)$ Rayleigh number	e E	east control volume face east grid point
Nu	$(=g\beta(T_{\rm h}-T_{\rm c})\hat{H}^3/\nu\alpha)$	h	hot wall
s, S	south face of a control volume; arc length; south neighbor of the P	i	condition at baffle-air interface; also neighbors of the P grid point
S <sup>Φ</sup> T	grid point; also distance along a wall source term dimensional temperature	max N, P, S, W	maximum value north, main, south, and west grid
u, U	dimensional and dimensionless x velocity		points, respectively
v, V	dimensional and dimensionless y velocity	Superscrip	pts
w, W	west face of a control volume,	•	previous iteration value
	west neighbor of the P grid point;	,	correction value
	also width of cavity	φ	refers to dependent variables

gated, and the effects of baffle height and location on the total heat transfer are determined. The physical situation is depicted in Figure 1a and, as described below, is relevant to heat transfer in attic spaces and industrial buildings.

Iyican et al. [2, 3] studied experimentally and analytically the natural convection motion and heat transfer within an inclined trapezoidal cavity formed from parallel cylindrical top and bottom walls that are maintained at different uniform temperatures and plane adiabatic side walls. The experimental and numerical investigations presented by Lam et al. [4] are for a trapezoidal cavity formed

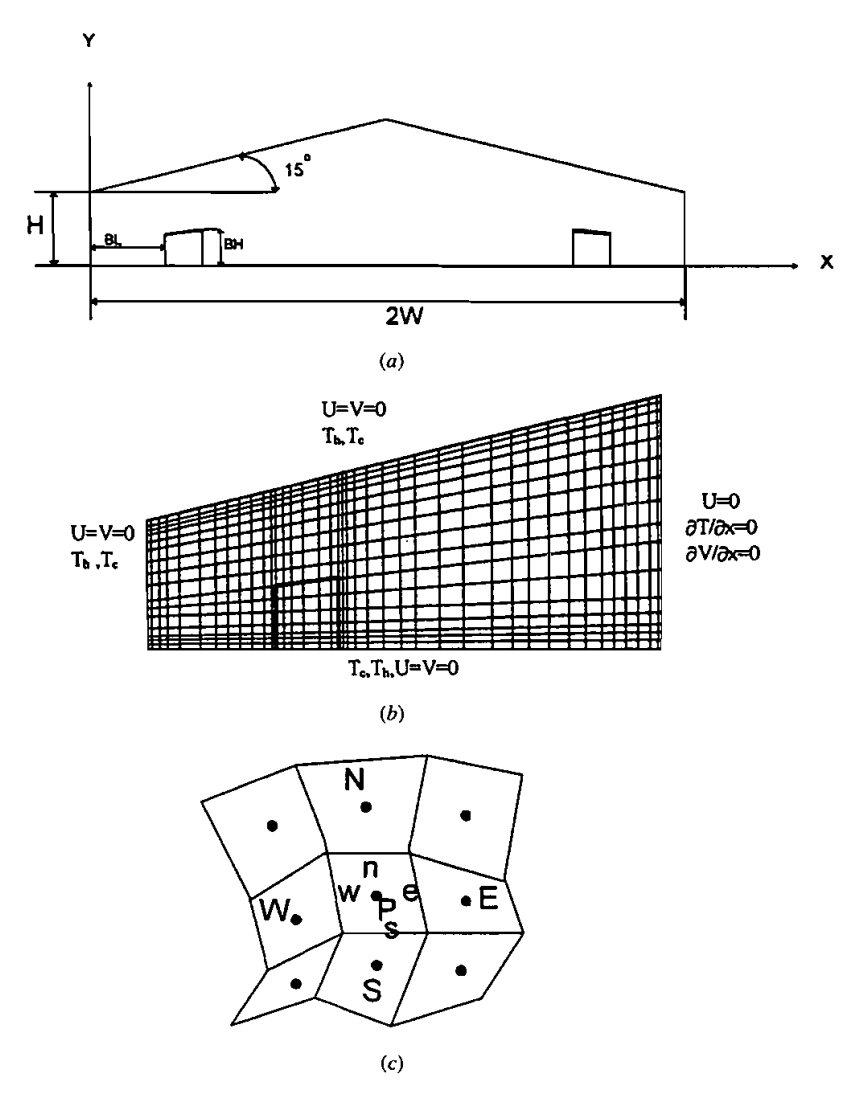


Figure 1. (a) Physical domain, (b) computational domain and an illustrative grid network, and (c) a typical control volume.

between two vertical adiabatic side walls, a horizontal hot bottom wall, and an inclined cold top wall. Results obtained indicated that a two-dimensional numerical analysis cannot describe the three-dimensional flows that occur in the bottom-heated cavity but it can predict heat transfer rates to an acceptable level of accuracy. Karyakin [5] performed a study on transient natural convection in prismatic enclosures of arbitrary cross section including a trapezoidal cavity with parallel top and bottom walls and inclined side walls.

The triangular cavity may be viewed as a special case of trapezoidal enclosures whose upper and lower surfaces are not parallel. Akinsete and Coleman [6]

obtained numerical predictions for natural convection in a triangular cavity that consists of adiabatic vertical walls, a horizontal bottom wall, and an inclined top wall. Results were presented for two different boundary conditions of uniform temperature and uniform heat flux along the horizontal and inclined walls. Bejan and Poulikakos [7] studied natural convection in an attic space filled with porous material. Poulikakos and Bejan [8, 9] analyzed theoretically and experimentally the fluid dynamics of an attic space. Transient heat transfer results in the same geometry were reported by Karyakin et al. [10].

In this article a control volume based numerical technique is used to generate results for the problem shown schematically in Figure 1a. The physical situation that this configuration represents is that of an attic space or an industrial building. Two boundary conditions are investigated. In the first, the bottom wall of the cavity is maintained at a uniform cold temperature  $T_c$  and all other walls are maintained at a uniform hot temperature  $T_h$ . This corresponds to, for example, conditions on a summer day in the attic, with all the vertical and top walls exposed to the hot ambient at an elevated temperature and the lower surface exposed to the airconditioned interior at a lower temperature. In the second, the bottom wall is hot  $(T_h)$ , while the temperature of all other walls is  $T_c$ . This configuration mimics wintertime conditions in the attic with the vertical and top walls exposed to the cold ambient and the lower surface adjoining the heated interior of the building. In both cases, the effects of mounting two symmetrically located baffles or partial dividers to the horizontal base of the enclosure, on the amount of heat transferred to an adjacent space (for example, to the interior of the building) are studied. Because of symmetry around the y axis, computations are performed in only half of the physical domain.

In the configuration studied the computational domain or the half-width of the cavity (W) is 4 times the height  $(\hat{H})$  of the short vertical wall. The inclination of the top of the cavity is fixed at 15°. Two baffle heights (BH = H/3 and 2H/3) and two baffle locations (BL = W/3 and 2W/3) are considered. In all computations the baffle thickness (BT) is taken as BT = W/20, to simulate a thin baffle.

#### **GOVERNING EQUATIONS**

The equations governing the flow and heat transfer are those that express the conservation of mass, momentum, and energy. The flow, driven by buoyant forces arising from variation in density within the enclosure, is assumed to be steady, laminar, and two-dimensional. Radiation is neglected in this study, and therefore results are applicable for moderate temperature differences. The Boussineq approximation is used to incorporate the temperature dependence of density in the conservation equations. In this approximation the density variations are only included in the body force term of the y momentum equation and are assumed to be a linear function of temperature. With these assumptions, the nondimensional mass, momentum, and energy equations become

$$\frac{\partial U}{\partial X} + \frac{\partial V}{\partial Y} = 0 \tag{1}$$

$$U\frac{\partial U}{\partial X} + V\frac{\partial U}{\partial Y} = -\frac{\partial P}{\partial X} + \frac{\partial^2 U}{\partial X^2} + \frac{\partial^2 U}{\partial Y^2}$$
 (2)

$$U\frac{\partial V}{\partial X} + V\frac{\partial V}{\partial Y} = -\frac{\partial P}{\partial Y} + \frac{\partial^2 V}{\partial X^2} + \frac{\partial^2 V}{\partial Y^2} + \frac{\operatorname{Ra}\theta}{\operatorname{Pr}}$$
(3)

$$U\frac{\partial\theta}{\partial X} + V\frac{\partial\theta}{\partial Y} = \frac{1}{\Pr}\left(\frac{\partial^2\theta}{\partial X^2} + \frac{\partial^2\theta}{\partial Y^2}\right) \tag{4}$$

where the following dimensionless variables have been used.

$$X = \frac{x}{\hat{H}} \qquad Y = \frac{y}{\hat{H}} \tag{5}$$

$$U = \frac{u}{v/\hat{H}} \qquad V = \frac{v}{v/\hat{H}} \tag{6}$$

$$P = \frac{p + \rho gy}{\rho \left(\nu/\hat{H}\right)^2} \qquad \theta = \frac{T - T_c}{T_h - T_c} \tag{7}$$

In the baffle the governing conservation equation is the dimensionless Laplace's equation, expressed as

$$\frac{k_{\rm b}/k}{\rm Pr} \left( \frac{\partial^2 \theta_{\rm b}}{\partial X^2} + \frac{\partial^2 \theta_{\rm b}}{\partial Y^2} \right) = 0 \tag{8}$$

where  $k_b/k = k_r$  is the dimensionless baffle conductivity and  $\theta_b$  denotes the temperature in the baffle region. The energy balance at the baffle-air interface can be stated as

$$-\frac{1}{\Pr}\left(\frac{\partial\theta}{\partial n}\right)_{i} = -\frac{k_{r}}{\Pr}\left(\frac{\partial\theta_{b}}{\partial n}\right)_{i} \tag{9}$$

where n denotes the direction normal to the baffle-air interface and the subscript i refers to the interface.

To close the system of equations, hydrodynamic and thermal boundary conditions are needed. Along the walls of the enclosure the velocity components are set to zero; the nondimensional wall temperature is specified to be 1 and 0 along the hot and cold walls, respectively (Figure 1b). The U velocity and the gradients of the remaining variables are set to zero along the symmetry line.

#### **SOLUTION PROCEDURE**

A nonstaggered curvilinear grid arrangement is used in solving the conservation equations, and the method of Rhie and Chow [11] that embodies the semi-implicit method for pressure linked equations (SIMPLE) algorithm of Patankar [12] is employed to suppress oscillatory checkerboard fields. The grid generation procedure along with the discretization of the conservation equations are briefly reviewed next. Additional details can be found in the works by Rhie and Chow [11] and Acharya and Moukalled [13].

#### **Grid Generation**

The curvilinear grid is generated by an algebraic method known as "transfinite mappings" or "transfinite interpolations" [14–16]. In this approach the mapping is done by using a bilinear shape function very similar to a finite element shape function. However, a special procedure is used to calculate the local coordinates of each internal grid point as a weighted function of the boundary points. The local coordinates are obtained from a linear interpolation procedure between the opposite boundary nodes for the east-west and north-south boundaries, respectively.

The above method requires that all the physical coordinates of the nodes on all four boundaries ( $\eta = \eta_{\min}$ ,  $\eta = \eta_{\max}$ ,  $\xi = \xi_{\min}$ ,  $\xi = \xi_{\max}$ ) of the solution domain be given. The proportionality factors are formed using the boundary grid points as follows:

$$f_{i,1}^{\xi} = \frac{x_{i,1} - x_{1,1}}{x_{ni,1} - x_{1,1}} \qquad f_{i,nj}^{\xi} = \frac{x_{i,nj} - x_{1,nj}}{x_{ni,nj} - x_{1,nj}} \tag{10}$$

$$f_{1,j}^{\eta} = \frac{y_{1,j} - y_{1,1}}{y_{1,n,i} - y_{1,1}} \qquad f_{ni,j}^{\eta} = \frac{y_{ni,j} - y_{ni,1}}{y_{ni,n,i} - y_{ni,1}}$$
(11)

The coordinates of the interior grid points are then calculated from the following interpolation formulae:

$$x_{i,j} = x_{1,j} + f_{i,j}^{\xi}(x_{ni,j} - x_{1,j})$$
 (12)

$$y_{i,j} = y_{i,1} + f_{i,j}^{\eta}(y_{i,nj} - y_{i,1})$$
(13)

where the values of functions  $f^{\xi}$  and  $f^{\eta}$  for the interior points are calculated by interpolating between the two boundary functions defined by Eqs. (10) and (11). The interpolation practice employed is as follows:

$$f_{i,j}^{\xi} = \frac{(nj-j)f_{i,1}^{\xi} + (j-1)f_{i,nj}^{\xi}}{nj-1}$$
 (14)

$$f_{i,j}^{\eta} = \frac{(ni-i)f_{1,j}^{\eta} + (i-1)f_{ni,j}^{\eta}}{ni-1}$$
 (15)

While generating the grid system, care was taken to make sure that the edges of the baffle lie along coordinate lines. An illustrative grid network generated is shown in Figure 1b.

#### Discretization of the Conservation Equations

The governing equations (Eqs. (1)-(4)) are first expressed in a general curvilinear coordinate system. If  $\phi$  represents a general scalar variable, its dimensionless conservation equation in curvilinear coordinates is given by

$$\frac{\partial}{\partial \xi} \left[ G_1 \phi - \frac{\Gamma^{\phi}}{J} \left( \alpha \frac{\partial \phi}{\partial \xi} - \beta \frac{\partial \phi}{\partial \eta} \right) \right] + \frac{\partial}{\partial \eta} \left[ G_2 \phi - \frac{\Gamma^{\phi}}{J} \left( \gamma \frac{\partial \phi}{\partial \eta} - \beta \frac{\partial \phi}{\partial \xi} \right) \right] = S^{\phi} J \tag{16}$$

where  $S^{\Phi}$  is the source term,  $\Gamma^{\phi}$  is the diffusion coefficient,  $G_1/J$  and  $G_2/J$  are the contravariant velocity components, and  $\alpha$ ,  $\beta$ , and  $\gamma$  are the metric quantities. The terms  $\alpha$ ,  $\beta$ ,  $\gamma$ ,  $G_1$ ,  $G_2$ , and J are defined by

$$\alpha = \left(\frac{\partial X}{\partial \eta}\right)^{2} + \left(\frac{\partial Y}{\partial \eta}\right)^{2} \qquad \beta = \left(\frac{\partial X}{\partial \xi}\right) \left(\frac{\partial X}{\partial \eta}\right) + \left(\frac{\partial Y}{\partial \xi}\right) \left(\frac{\partial Y}{\partial \eta}\right)$$

$$\gamma = \left(\frac{\partial X}{\partial \xi}\right)^{2} + \left(\frac{\partial Y}{\partial \xi}\right)^{2}$$
(17)

$$G_1 = U \frac{\partial Y}{\partial \eta} - V \frac{\partial X}{\partial \eta} \qquad G_2 = V \frac{\partial X}{\partial \xi} - U \frac{\partial Y}{\partial \xi} \qquad J = \frac{\partial X}{\partial \xi} \frac{\partial Y}{\partial \eta} - \frac{\partial X}{\partial \eta} \frac{\partial Y}{\partial \xi}$$
 (18)

Since the control volume approach is adopted, the physical domain is subdivided into a number of control volumes (Figure 1c), each associated with a grid point. The discretized form is obtained by integrating Eq. (16) over the control volume shown in Figure 1c along with suitable interpolation expressions for the variables at the control volume faces. This leads to the following general form of the conservation equation for  $\phi$ 

$$a_{\rm p}\phi_{\rm p} = a_{\rm E}\phi_{\rm E} + a_{\rm W}\phi_{\rm W} + a_{\rm N}\phi_{\rm N} + a_{\rm S}\phi_{\rm S} + S_{\rm P}^{\phi}$$
 (19)

The subscripts P, E, W, N, and S refer to the grid point at the center of the control volume and the four neighboring grid points, respectively. The term  $S_P^{\phi}$  includes the original source term in the equation, plus the contribution due to nonorthogonality of the grid system used.

The unknown pressure field is obtained using a guess-and-correct procedure similar to that described by the SIMPLE algorithm of Patankar [12], in which a pressure-correction  $(p' = p - p^*)$  equation is derived by combining the momentum and continuity equations. The source term of the p' equation contains the sum of the interface mass flow rates and represents the local mass imbalance. Spurious oscillations in the predicted solutions are suppressed by adding the following stabilization term to  $G^*$  in the source term of the pressure-correction

equation [11]:

$$(G_1^*)_{\rm e} = \left(\overline{G_1^*}\right)_{\rm e} + \overline{B} \left\{ \frac{P_{\rm E} - P_{\rm P}}{\delta \xi} - \overline{P} \xi \right\}$$
 (20)

The overbar in the equation indicates that the results are obtained by linear interpolation between grid nodes, and B depends on the metric quantities and the coefficients. This practice ((Eq. (20)) has been found to successfully suppress spurious oscillatory pressure and velocity fields.

#### **Computational Details and Numerical Accuracy**

The presence of baffles is accounted for in the momentum equations by specifying a very high  $a_P$  coefficient ( $\sim 10^{30}$ ) in the baffle region. When solving the energy equation, the dimensionless baffle conductivity is set to  $k_r^r/Pr$ . This specification of a high  $a_p$ , in addition to the no-slip boundary condition, suppresses the velocities in the baffle to vanishing values. Thus in the baffle region, Eq. (4) is reduced to the appropriate Laplace's equation (Eq. (8)). Further, since the numerical scheme is conservative, flux leaving a control volume through one face is exactly equal to the flux entering the adjacent control volume through the same face. Thus the interface energy balance (Eq. (9)) is exactly satisfied at the baffle-air interface. Furthermore, because of the high values of  $a_P$  (~10<sup>30</sup>), the coefficients of the discretized velocity equation in the baffle region are very high ( $\sim 10^{30}$ ), and since the coefficients in the pressure-correction equation are inversely proportional to the coefficients in the velocity equations, the coefficients of P' in the baffle region are nearly zero. Therefore the pressure-correction field in the fluid is independent of the P' values in the baffle. Thus incorrect pressure-correction fields are avoided.

A grid independent solution was obtained with a  $120 \times 120$  mesh size. A nonuniform grid was used in order to concentrate grid nodes in regions where large gradients of the flow variables were expected. This practice was adopted near the walls and symmetry lines. The accuracy of the solution presented in this article was checked by direct comparison with the solution generated on a  $160 \times 160$ nearly uniform grid. The maximum difference in the various quantities predicted was less than 0.69%. Conservation of mass, momentum, and energy were found to be satisfied to within 0.001% in each control volume. Comparisons were also made with results generated using the well-known FLOW-3D commercial computational fluid dynamics (CFD) code. The difference in the average Nusselt numbers for the cases studied was less than 0.05%. A three-dimensional version of the problem was also solved using FLOW-3D, for a few cases, for the boundary condition representing summertime situations. The maximum difference in the average Nusselt number between the two- and three-dimensional computations was within acceptable limits (less than 5.84%), given the coarseness of the grid used in the three-dimensional computations. In fact, streamline plots revealed that the problem is actually two-dimensional. As a further check for accuracy, computations were performed for a nonpartitioned trapezoidal cavity using the boundary conditions of Lam et al. [4]. The two solutions compared very well with each other, with the streamline and isotherm maps computed in this work falling right on top of the plotted streamline and isotherm maps of Lam et al. [4].

#### **RESULTS AND DISCUSSION**

An examination of the dimensionless governing equations reveals three flow parameters for each of the two boundary conditions employed: the Prandtl number Pr, the Rayleigh number Ra, and the conductivity ratio  $k_r$ . The Prandtl number is assigned the value of 0.72 corresponding to air, the Rayleigh number values are varied between  $10^3$  and  $5 \times 10^7$  for summertime boundary conditions and between  $10^3$  and  $10^6$  for wintertime boundary conditions, and the conductivity ratio is assigned the value of 2 to simulate a poorly conducting baffle. In addition to the aforementioned parameters, there are two geometric parameters: the baffle height (BH) and the baffle location (BL). As noted earlier, two different baffle heights (BH = H/3 and 2H/3) and two different baffle locations (BL = W/3 and 2W/3) are studied.

Results presented next are displayed in the form of streamlines, isotherms, midwidth U velocity and temperature profiles, and the local and average Nusselt number values.

#### **Summertime Boundary Conditions**

**Streamlines and isotherms.** Representative flow patterns and temperature distributions are shown in Figures 2-4 and the maximum absolute values of the stream function ( $|\Psi_{max}|$ ) are displayed in Table 1. In Figure 2, streamlines and isotherms are presented in a baffle-free enclosure for different values of Rayleigh number (Ra =  $10^4$ - $10^7$ ). The flow consists of a recirculating eddy rotating clockwise, indicating that air is moving up along the heated wall, down along the symmetry line, and horizontally to the left along the cold base of the trapezoidal cavity. The eye of the recirculation is close to the vertical hot wall of the enclosure,

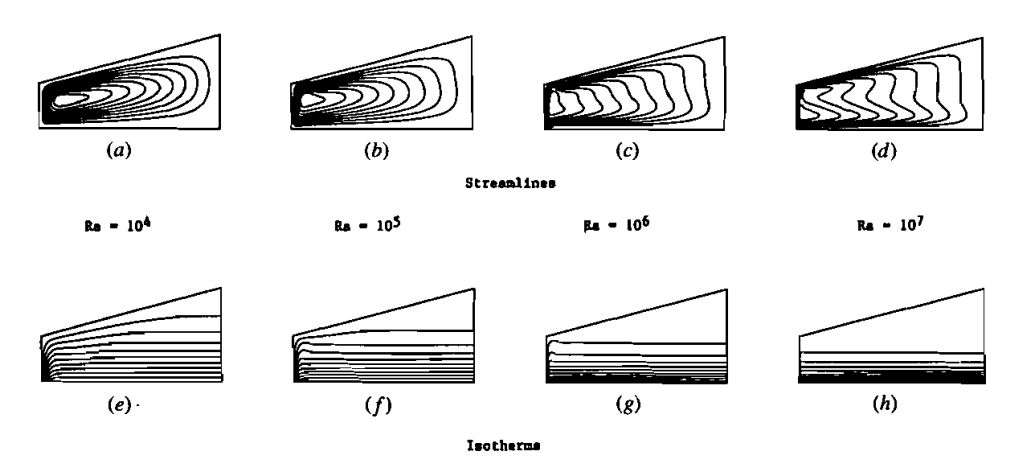


Figure 2. Streamline and isotherm plots in a nonpartitioned cavity (summer).

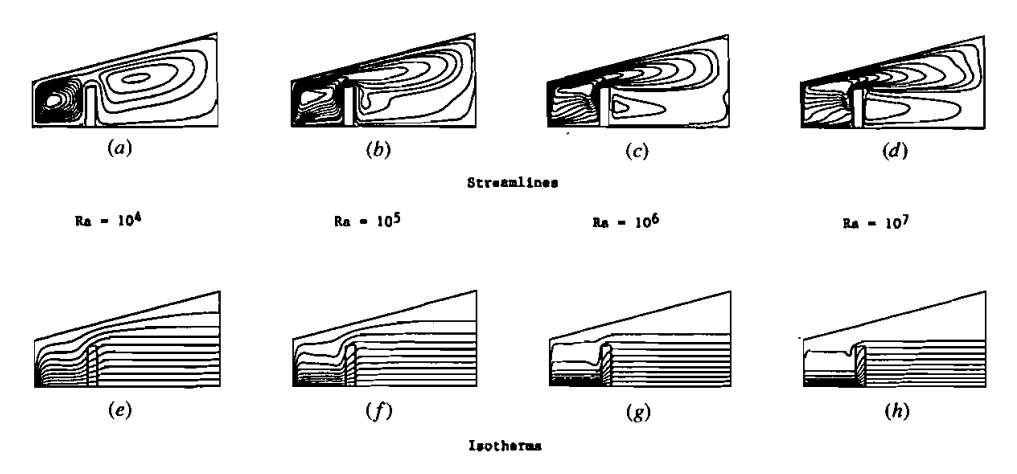


Figure 3. Streamline and isotherm plots for BL = W/3 and BH = 2H/3 (summer).

where the largest velocities are located. As Ra increases, the eye moves further downward and toward the lower corner of the hot wall, and the intensity of convection in the upper part of the domain close to the symmetry line decreases (Figures 2a-2d).

At low Ra, isotherms are uniformly distributed over the domain (Figure 2e), implying weak convection effects. As Ra increases, the temperature distribution in the upper portion of the enclosure approaches the conditions of thermal stratification (Figures 2f-2h). In this region, buoyancy forces are small, as are the heat fluxes through the inclined wall. Furthermore, isotherms reveal that convection heat transfer is mainly from the vertical hot wall along which a thermal plume of increasing strength rises.

The effect of baffles on flow patterns and temperature distributions is shown in Figure 3 for BH = 2H/3, BL = W/3 and in Figure 4 for BH = H/3, BL =

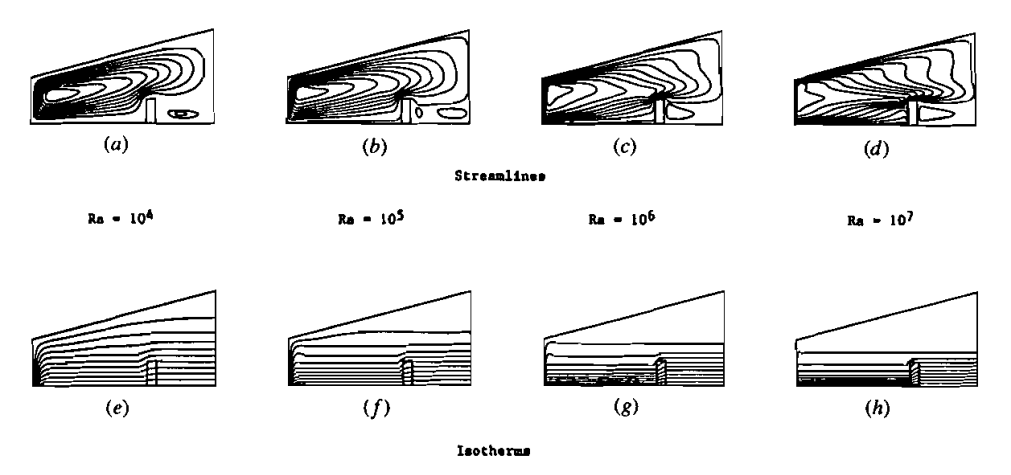


Figure 4. Streamline and isotherm plots for BL = 2W/3 and BH = H/3 (summer).

Ra	BH = 0 BL = 0	BH = H/3		BH = 2H/3	
		BL = W/3	BL = 2W/3	BL = W/3	BL = 2W/3
103	1.42	1.18	1.39	1.06	1.35
10 <sup>4</sup>	5.66	5.23	5.56	3.99	5.24
10 <sup>5</sup>	11.61	12.01	11.66	9.29	10.95
10 <sup>6</sup>	17.02	19.85	18.02	21.31	16.52
10 <sup>7</sup>	23.45	29.129	24.36	37.40	26.43
$5 \times 10^7$	27.63	39.05	28.97	47.83	125.05

Table 1. Maximum absolute values of the stream function for summertime conditions

2W/3. The results in Figure 3 indicate that at the lowest Ra presented (Ra =  $10^4$ ), the recirculating flow exhibits two vortex cores within one overall large rotating eddy (Figure 3a). These two inner vortices rotate in the clockwise direction. As Ra increases (Ra =  $10^5$ ), the two vortices merge into one (Figure 3b). Further increases in Ra (Ra =  $10^6$  and  $10^7$ , Figures 3c and 3d) result in flow separation between the baffle and the symmetry centerline.

To explain the above behavior, it should be noted that as the flow rises along the heated vertical and then the heated inclined wall, it gets stratified. At low Ra the flow moving down the right symmetry line is not sufficiently stratified and is therefore able to negotiate into the lower right cavity. At higher Ra (10<sup>6</sup>, 10<sup>7</sup>) the right portion of the cavity is fully stratified, and the flow is no longer able to penetrate the lower right cavity. Consequently, the flow separates from the symmetry line at a location that corresponds to the baffle height, and a jet-like flow directed from the symmetry line to the baffle tip is observed. This behavior has been observed earlier computationally [17] and experimentally [18] in rectangular enclosures with isothermal vertical walls and adiabatic horizontal walls. As a consequence of this flow separation, a counterclockwise eddy, primarily shear-driven, is formed in the lower right cavity.

Isotherms presented in Figures 3e-3h reflect the above described flow patterns. At a low Ra, variations in temperature are almost uniform over the domain, indicating dominant conduction heat transfer mode. As Ra increases, convection is promoted, and isotherms are distorted. Along the inclined hot wall, the heat fluxes are small and decrease with increasing Ra. In this region the fluid has a homogeneous temperature and is thermally stratified. Along the cold base of the enclosure, temperature gradients to the left of the baffle are higher (i.e., isotherms are closely packed) than those to the right because of stronger convection-induced flows.

Streamline and isotherm maps for BH = H/3 (shorter baffle) placed at BL = 2W/3 (closer to the symmetry line) are shown in Figure 4 and reveal essentially the above discussed behavior with the exception of the flow separation from the symmetry line occurring even at the lowest Ra. Furthermore, comparison of streamlines and isotherms presented in Figures 3 and 4 indicates a stronger convective flow for the case when BH = 2H/3 and BL = W/3, but for BH = H/3 and BL = 2W/3 the area covered by the strong convective eddy is larger. This is

further revealed in Table 1, where  $|\Psi_{max}|$  is shown to increase with increasing BH, decreasing BL, and increasing Ra. As will be shown below, this increase in  $|\Psi_{max}|$  does not necessarily mean an increase in the total heat transfer because it is associated with a smaller effective convection area.

The partitions appear to decrease the isothermal stratification near the top inclined wall. This is evidenced by the larger isothermal region in the isotherms of Figure 2, compared to the isotherms in Figure 3 and 4. A similar comparison of the streamlines indicates an increase in the flow velocity along the inclined wall in the presence of the partitions.

Velocity and temperature profiles. The variations of the horizontal velocity component and the temperature profiles along  $X = W/2\hat{H}$  are shown in Figures 5 and 6, respectively, for a nonpartitioned cavity and for a partitioned one for which BL = W/3 and BH = 2H/3. The velocity profiles in general reflect the flow patterns displayed in Figure 2. Near the hot upper wall the velocity profiles are steeper for the partitioned cavity as compared to those in the nonpartitioned cavity. However, the opposite is true near the cold wall, where for the partitioned case the region is characterized by stratification and flow separation. Near the cold wall the velocities are therefore very small for the partitioned cavity, indicating weak convection in that region (to the right of the baffle). At  $Ra = 10^7$  the flow separation from the symmetry line along the baffle tip can be clearly seen with large negative U velocities near the tip and small positive velocities in the counterclockwise eddy behind the baffle. However, both at  $Ra = 10^5$  and  $10^7$ , the velocity very close to the cold wall is negative, implying that some fraction of the primary clockwise eddy is able to penetrate down to the cold wall. The temperature profiles (Figure 6) indicate the increasing stratification near the top wall with

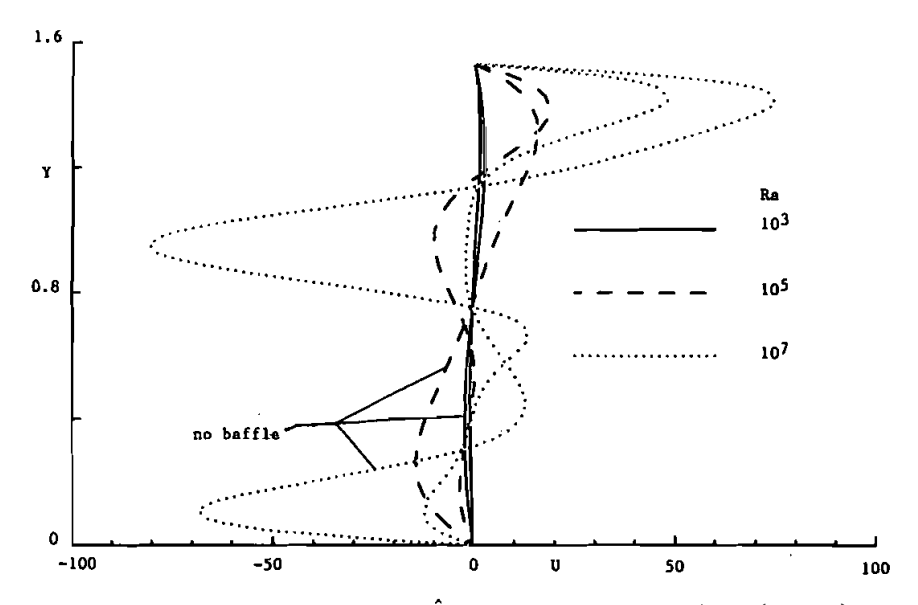


Figure 5. Velocity profiles at  $X = W/2\hat{H}$  for BL = W/3 and BH = 2H/3 (summer).

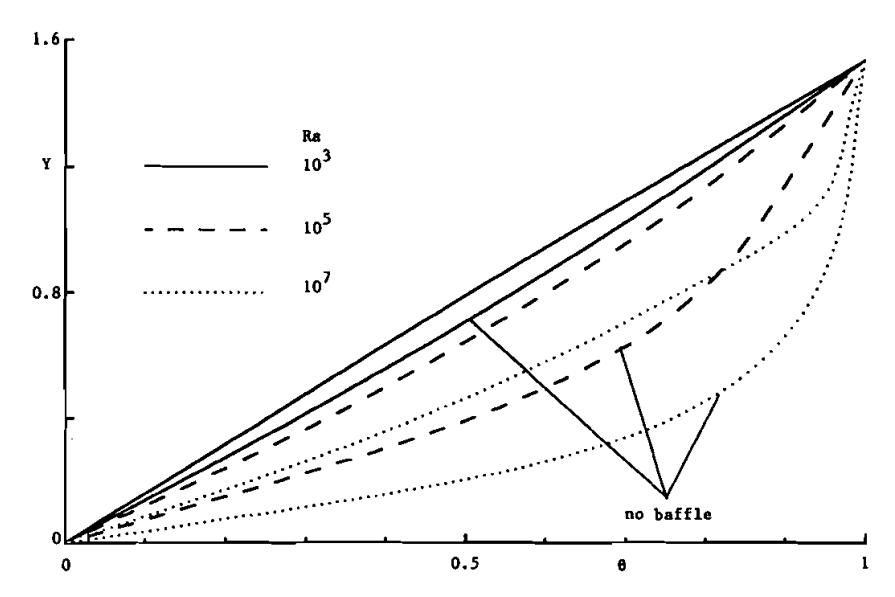


Figure 6. Temperature profiles at  $X = W/2\hat{H}$  for BL = W/3 and BH = 2H/3 (summer).

increasing Ra. As for the velocity gradients, for a partitioned cavity, temperature gradients are higher near the hot wall and lower near the cold wall as compared to values obtained for a nonpartitioned cavity. This implies that the baffles increase the heat transfer from the upper (inclined) heated surface and decrease it along the lower cooled surface. The latter effect (reduced heat gain) is clearly desirable in summertime conditions.

**Nusselt numbers.** The local heat transfer coefficient and the Nusselt number along the hot and cold walls are computed using the following definitions:

$$h_{\rm h} = -\frac{k(\partial T/\partial n)]_{\rm h}}{(T_{\rm h} - T_{\rm c})} \qquad h_{\rm c} = -\frac{k(\partial T/\partial n)]_{\rm c}}{(T_{\rm h} - T_{\rm c})} \tag{21}$$

$$Nu_{h} = \frac{h_{h}S_{h, max}}{k} \qquad Nu_{c} = \frac{h_{c}S_{c, max}}{k}$$
 (22)

where n denotes the normal distance from the wall and S is the distance along the heated or cooled wall measured from its lowest point (X = 0, Y = 0). The average heat transfer coefficients and Nusselt numbers are calculated as

$$\overline{h_h} = \frac{Q_{\text{conv}}}{A_h(T_h - T_c)} \qquad \overline{h_c} = -\frac{Q_{\text{conv}}}{A_c(T_h - T_c)}$$
 (23)

$$\overline{Nu_h} = \frac{\overline{h_h}S_{h, max}}{k} \qquad \overline{Nu_c} = \frac{\overline{h_c}S_{c, max}}{k}$$
 (24)

where  $Q_{\text{conv}}$  is the overall convection heat transfer at the surface and  $A_h$  and  $A_c$  are the heat transfer areas along the hot and cold walls, respectively. Since  $\overline{h}_h S_{h, \text{max}} = \overline{h}_c S_{c, \text{max}}$ , it follows that  $\overline{N} u_h = \overline{N} u_c = \overline{N} u$ .

The normalized local Nusselt number distribution  $Nu^*$  ( $Nu^* = Nu/Nu_0$ , where  $Nu_0$  is the value of Nusselt number for pure conduction, i.e., Ra = 0) along the hot and cold walls are presented for a partition-free enclosure and a partitioned enclosure (BL = W/3 and BH = 2H/3) in Figures 7 and 8, respectively. In this normalized form the relative effect of convection can be directly assessed. Values are plotted as a function of  $S/S_{max}$ , where  $S_{max}$  is the maximum possible value of S along the wall.

In Figure 7 the variations of Nu\* along the hot wall are presented. At low Ra, conduction is the dominant heat transfer mode in the whole enclosure (Nu<sub>h</sub>\* = 1). At high Ra and along the vertical portion of the hot wall (i.e.,  $S_h/S_{h,max} < 0.1945$ ), convection is the dominant heat transfer mode (Nu\* > 1) for both the partitioned and nonpartitioned enclosures, and Nu\* increases with increasing Ra values. Along the inclined portion of the hot wall (1 >  $S_h/S_{h,max} > 0.1945$ ), Nu\* < 1 along most of its length, and this is caused by the strong stratification effects in the upper region. As shown in Figure 7, the Nu ratio decreases all the way to the apex of the enclosure, reaching values as low as 0.02.

The effect of the baffles is to decrease heat transfer along the initial portion of the hot wall and to increase it along the remaining portion (Figure 7). The decrease in the initial part is due to the shift in the location of the vortex core from the lower to the upper left part of the domain (compare streamlines in Figures 2 and 3). The increase over the remaining portion of the hot wall is due to the larger temperature gradients caused by lower stratification levels (compare isotherms in Figures 2 and 3).

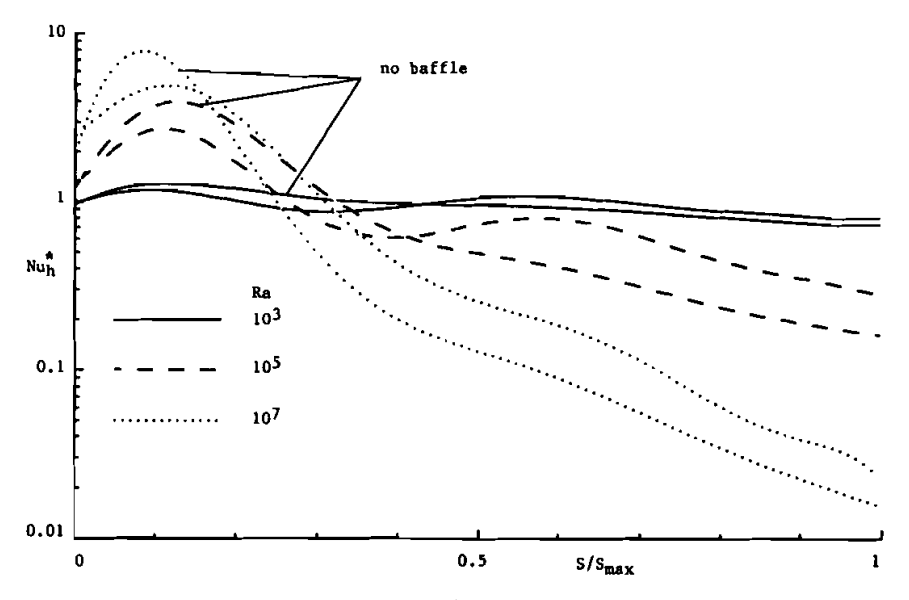


Figure 7. Local normalized Nusselt number distribution along the hot wall for BL = W/3 and BH = 2H/3 (summer).

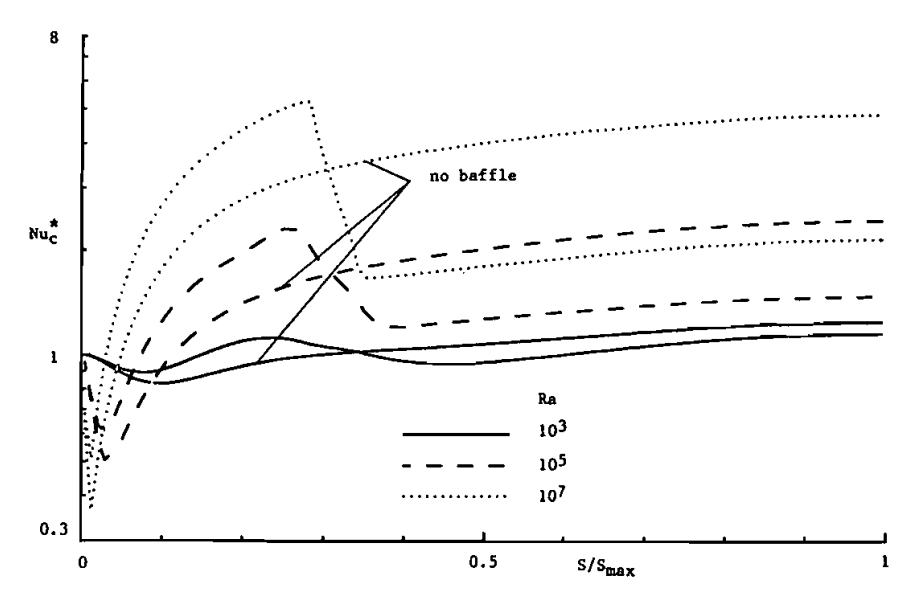


Figure 8. Local normalized Nusselt number distribution along the cold wall for BL = W/3 and BH = 2H/3 (summer).

The Nu distributions along the horizontal cold wall are displayed in Figure 8. As expected, the level of Nu increases with increasing Ra value. In a baffle-free enclosure the values of Nu decrease monotonically from right to left along the cold wall (except very close to the corner, where there is an increase due to the proximity of the heated wall). This is expected and is caused by the decease in the temperature of the fluid as it moves along the cold wall. In a partitioned enclosure the flow separates in the right portion of the domain. This flow separation leads to a separate counterrotating eddy in the right-trap region at higher Ra values and is associated with a decrease in heat transfer (Nusselt number) in that region as compared to values obtained in a nonpartitioned enclosure. The fluid reaching the portion of the cold wall to the left of the baffle is carried by the separated shear layer from the symmetry line and is therefore hotter than its counterpart in a nonpartitioned enclosure. Consequently, as depicted in Figure 8, the temperature gradients (and thus the Nusselt numbers) along that portion are higher for a partitioned enclosure. Note the very sharp increase in Nu<sup>\*</sup><sub>c</sub> across the baffle, which attests to the effect of the separated jet that impinges first on the top of the baffle and then moves down to the cold wall.

The normalized average Nu values ( $\overline{\text{Nu}}^*$ ) and the average conduction values ( $\overline{\text{Nu}}_0$ ) for all cases studied are given in Tables 2 and 3, respectively. At low and moderate Ra ( $<10^5$ ) the overall heat transfer appears to be strongly dominated by conduction. The contribution of advection to the total heat transfer becomes as important as the conduction contribution at Ra between  $10^6$  and  $10^7$ . In general, the presence of baffles decrease the overall heat transfer. The decrease in heat transfer is greater with increasing BH (baffle height) and decreasing BL (distance from the hot vertical wall). The average Nu values, displayed in normalized form in Table 2, are correlated with a maximum deviation of less than  $\pm 12.52\%$  via the

106

 $10^{7}$ 

 $5 \times 10^7$ 

Ra	BH = 0	BH = H/3		BH = 2H/3	
	BL = 0	BL = W/3	BL = 2W/3	BL = W/3	BL = 2W/3
10 <sup>3</sup>	1.010	1.007	1.008	1.007	1.008
104	1.107	1.076	1.100	1.0632	1.090
10 <sup>5</sup>	1.307	1.255	1.296	1.189	1.266

1.627

2.117

2.451

Table 2. Normalized average Nusselt number values (Nu\*) for summertime conditions

1.547

1.955

2.234

following relation:

1.659

2.191

2.519

$$\overline{\text{Nu}}^* = 3.03(\text{Ra})^{0.0803} \left(1 + \frac{\text{BL}}{W}\right)^{0.058} \left(1 + \frac{\text{BH}}{H}\right)^{-0.23}$$
 (25)

1.443

1.804

2.034

1.588

2.061

2.333

#### Wintertime Boundary Conditions

Streamlines and isotherms. Streamline and isotherm maps are displayed in Figures 9-11, while the maximum absolute values of the stream function  $|\Psi_{max}|$ are depicted in Table 4. Inspection of the computed streamlines and isotherms in the nonpartitioned enclosure (Figure 9) indicates that for  $Ra > 10^3$  the flow is composed of two counterclockwise rotating convective cells at the two ends with a third middle cell rotating clockwise. These findings are in line with those reported by Lam et al. [4] and Salmun [19]. Moreover, isotherm plots reveal that conduction is the dominant heat transfer mode at the lowest Ra considered (Figure 10e) and convection starts to dominate at values of Ra higher than 10<sup>3</sup>, as clearly seen by the distortion in the isotherms displayed in Figures 10f-10h. It should be pointed out here that a two-dimensional model cannot adequately describe the threedimensional flows that occur in the trapezoidal cavity under this given boundary condition; however, the two-dimensional model can predict, as demonstrated by Lam et al. [4], heat transfer rates to an acceptable accuracy. Since the intention here is to estimate and correlate heat transfer, the two-dimensional model used is perhaps sufficient.

Table 3. Average conduction Nusselt number values (Nu<sub>0</sub>) for summer and winter conditions

	Nu <sub>0</sub>
BH = 0, BL = 0	5.49204
BH = H/3	
BL = W/3	5.53837
BL = 2W/3	5.52636
BH = 2H/3	
BL = W/3	5.59128
BL = 2W/3	5.56778

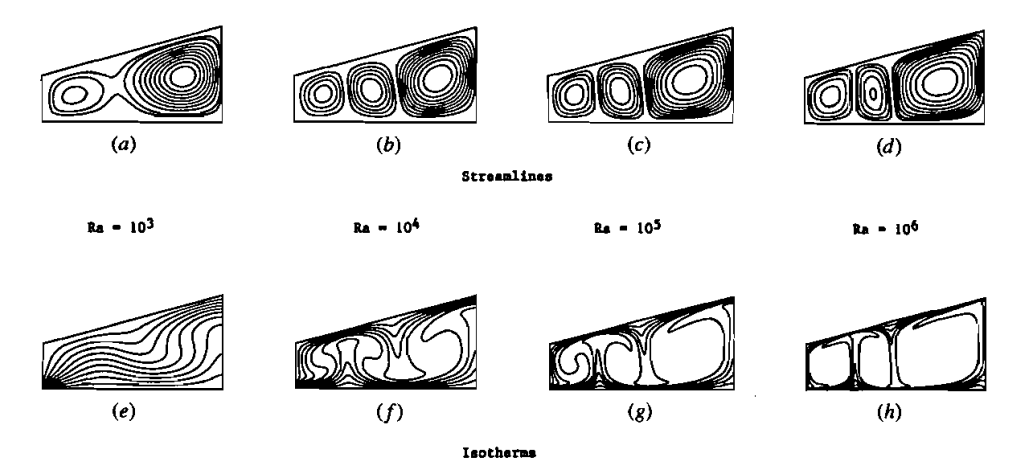


Figure 9. Streamline and isotherm plots in a nonpartitioned cavity (winter).

Results are presented in Figures 10 and 11 for partitioned enclosures. In Figure 10 the baffle height is BH = 2H/3 and is located at BL = W/3, while in Figure 11 the baffle height is BH = H/3 and is located at BL = 2W/3. As depicted, the presence of baffles significantly alters the flow and temperature fields. At low values of Ra ( $10^3$  and  $10^4$ ), streamlines and isotherms displayed in Figure 10 are slightly different from those shown in Figure 9, however, they are very different at high Ra ( $10^5$  and  $10^6$ ), where the number of large convective cells spanning the full vertical extent of the domain is reduced by 1. Small satellite cells appear for each of the two main large cells. At all Ra, for the tall baffle, there is little communication between the two sides.

For the configuration in Figure 11 (shorter baffle, placed further away from the hot wall) the flow pattern undergoes a transformation from a two-cell arrange-

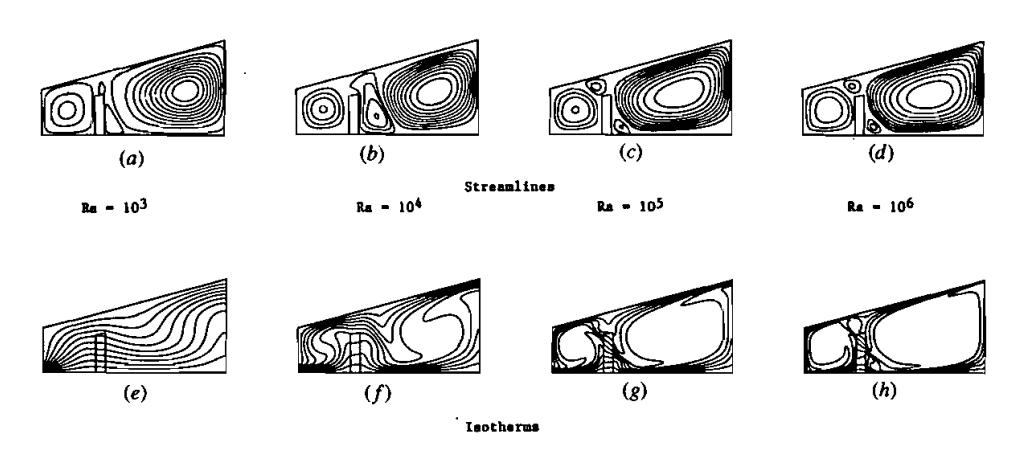


Figure 10. Streamline and isotherm plots for BL = W/3 and BH = 2H/3 (winter).

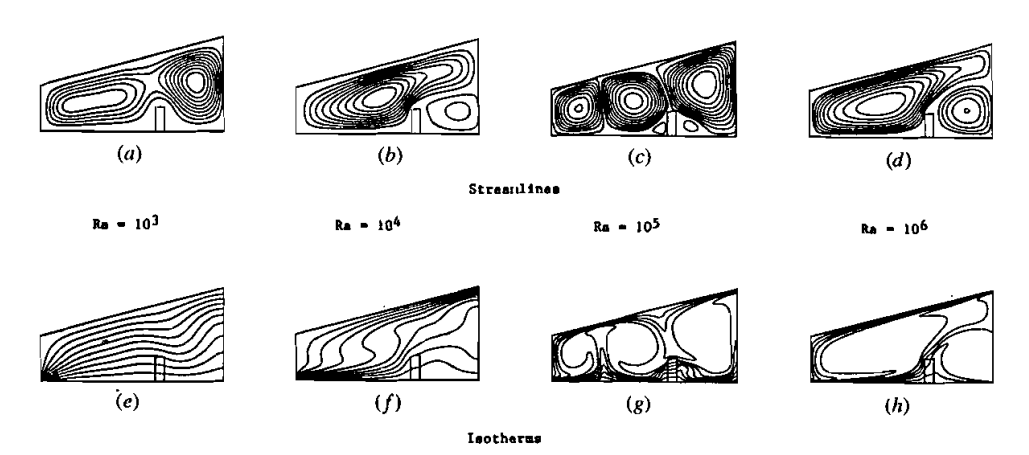


Figure 11. Streamline and isotherm plots for BL = 2W/3 and BH = H/3 (winter).

ment at  $Ra = 10^3$  to a three-cell pattern at  $Ra = 10^5$  and then back to a two-cell pattern at  $Ra = 10^6$ . This behavior is linked to the competing effects of the vertical cold wall that promote the flow pattern in Figure 11b and a heated bottom wall that promotes the flow pattern in Figure 11c. The cold wall at the top, because of its inclination, is likely to support both flow pattern modes. The isotherms mimic the flow behavior. Note the plume type isotherm patterns in Figure 11g and the boundary layer type isotherms in Figure 11h and their direct correspondence with the flow pattern.

Table 4 presents the maximum absolute value of the stream function  $|\Psi_{\text{max}}|$ , which is seen to be lower for a partitioned enclosure. By a careful inspection of Table 4, the following conclusions can be drawn: (1) for any Ra, partitions reduce  $|\Psi_{\text{max}}|$ , the largest reductions being for the partition that is farther away from the vertical wall; (2) the location of the partition influences the flow strength more so than does the height of the partition; and (3) at constant Ra the lowest  $|\Psi_{\text{max}}|$  is obtained for the configuration where BL = 2W/3 and BH = 2H/3.

**Velocity and temperature profiles.** Figure 12 shows the horizontal velocity component along X = W/2H for a nonpartitioned cavity and a partitioned one with a baffle of height BH = H/3 located at BL = 2W/3. The velocity profiles reflect the flow fields displayed in Figures 9 and 11. As expected, the magnitude of

Table 4. Maximum absolute values of the stream function for winter conditions

Ra	BH = 0 $BL = 0$	BH = H/3		BH = 2H/3	
		BL = W/3	BL = 2W/3	BL = W/3	BL = 2W/3
103	7.72	5.82	2.91	5.91	2.35
10 <sup>4</sup>	35.15	33.86	24.37	33.85	21.48
105	107.97	90.18	72.31	103.93	68.63
10 <sup>6</sup>	318.35	243.94	250.10	300.63	206.74

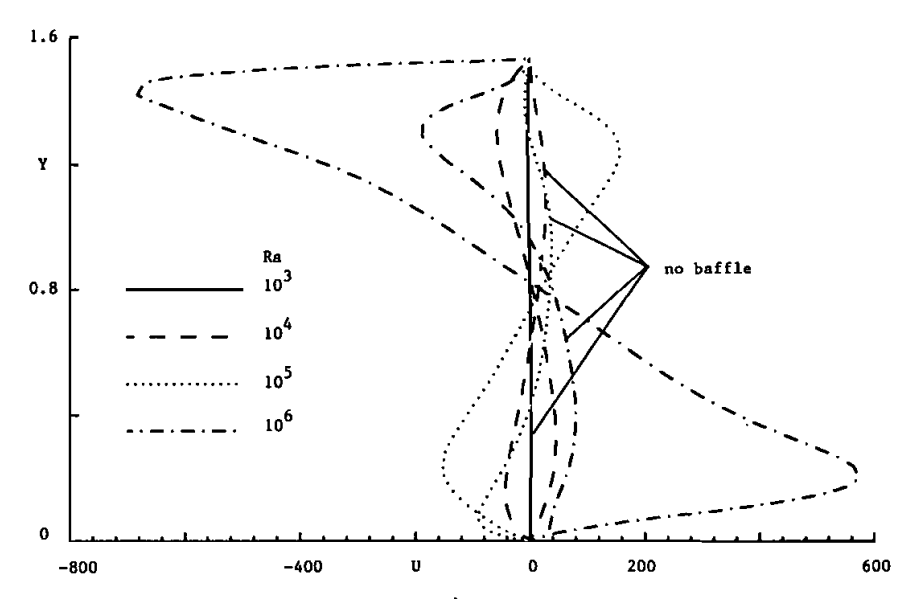


Figure 12. Velocity profiles at  $X = W/2\hat{H}$  for BL = 2W/3 and BH = H/3 (winter).

the horizontal velocity component increase with increasing Ra. Note the opposite direction of the velocities near the walls between the partitioned and nonpartitioned cases at  $Ra = 10^4$ , while at  $Ra = 10^5$ , the velocities appear to be in the same direction. This behavior is again linked to the differing flow patterns (two-cell versus three-cell) observed at different Ra.

The midwidth temperature profiles (X = W/2H) are shown, for the same configuration, in Figure 13. Again these profiles reflect the isotherm maps presented in Figures 9 and 11. The temperature distribution changes greatly from the conduction regime (i.e., linear distribution) at low Ra to the convection regime at high Ra. Furthermore, at high Ra the temperature profiles indicate the presence of two thermal boundary layers along the hot and cold walls where sharp gradients are observed. Because of the lower velocities and the strong stratification, the temperature gradients in the core are very small at high Ra. This is more pronounced in a partitioned enclosure. Furthermore, at high Ra there is clear evidence of temperature inversion near both the hot and cold walls.

**Nusselt numbers.** The local heat transfer coefficient and Nu along the hot and cold walls are computed using Eqs. (23) and (24). The normalized local Nu distributions Nu\* are shown for a nonpartitioned and a partitioned enclosure (BL = 2W/3 and BH = H/33) in Figures 14 and 15. In Figure 14 the variations of Nu\* along the bottom hot wall are presented. For a nonpartitioned enclosure the same trend is observed at all values of Ra considered with an increase in the level of Nu\* (i.e., in convection heat transfer) with increasing Ra. As depicted, a dual peak in the normalized Nu is noticed. As the flow proceeds to the right, away from the vertical cold wall, the heat transfer increases until it reaches a maximum at  $X \approx 0.15$  and then starts decreasing to reach a minimum at  $X \approx 0.25-0.3$ , where the thermal plumes induced by the left and middle eddies rise upward, away from

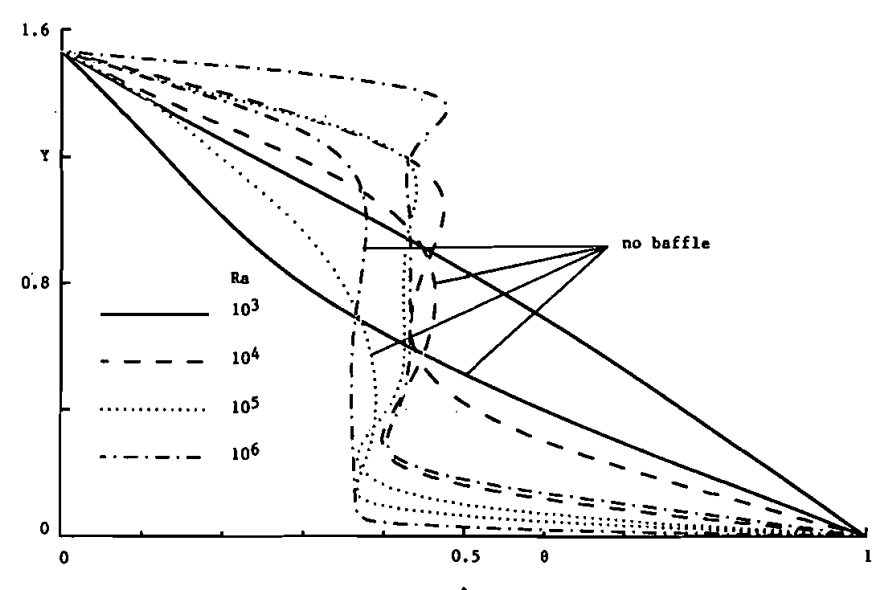


Figure 13. Temperature profiles at  $X = W/2\hat{H}$  for BL = 2W/3 and BH = H/3 (winter).

the hot surface, creating a region of low temperature gradients (see Figures 9f-9h) and therefore low Nu\*. The second peak is caused by the impingement of the cold streams from the middle and right eddy on the hot wall at  $X \approx 0.5$ , creating large temperature gradients and thereby large Nu\*. The decrease to the left and right of the second peak is due to the increase in the temperature of the cold fluid, which decreases the temperature gradients and leads to lower heat transfer.

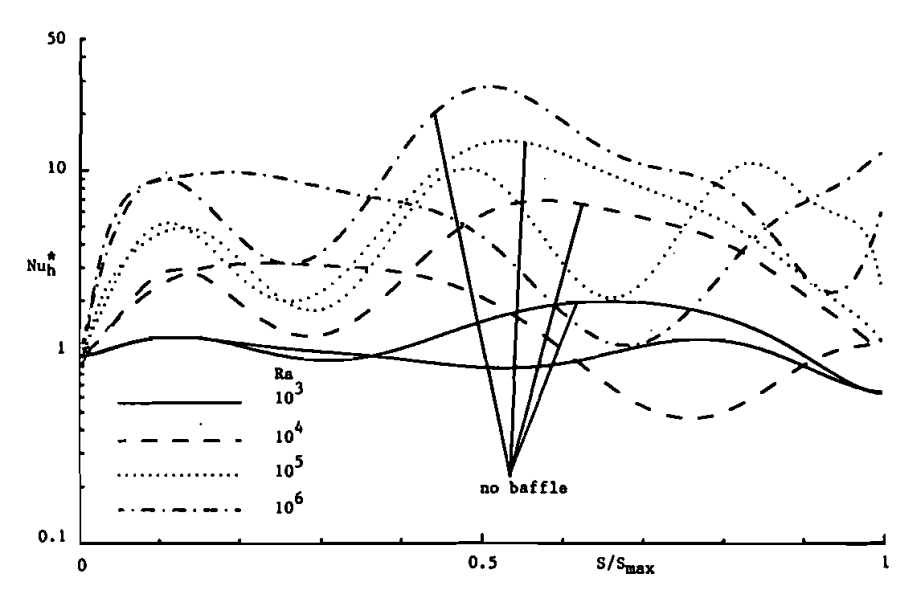


Figure 14. Local normalized Nusselt number distribution along the hot wall for BL = 2W/3 and BH = H/3 (winter).

In the presence of baffles, the level of Nu\* for the same value of Ra decreases, indicating a decrease in total heat transfer. For the cases where convection is the dominant heat transfer mode (i.e., for Ra  $\geq 10^4$ ), a local minimum (depression) in Nu\* is observed at the location of the baffle. Flow separates on both sides of the baffle (Figure 11c, for example), leading to small relatively weak baffle-corner recirculation regions, and these are associated with low heat transfer rates. Elsewhere along the hot wall, Nu\* distribution reflects the flow patterns and isotherms displayed in Figure 11. Depending on the number of cells, two or three peaks are observed. For Ra =  $10^4$  and  $10^6$ , where there are two primary cells, one peak is observed where the cold flow moving down the vertical wall impinges on the heated surface, and the other peak is associated with the location where the smaller second eddy to the right of the baffle impinges along the hot wall (near the symmetry line). For Ra =  $10^5$ , three primary eddies are seen, as in the nonpartitioned case, and correspondingly, three peaks are noted.

The normalized Nu distributions along the cold wall are displayed in Figure 15. In a baffle-free enclosure the Nu distributions correspond to the three-roll pattern. Starting from the top most point (i.e.,  $S_c/S_{c,max}=1$ ) and moving to the left, Nu\* decreases because of a decrease in the temperature of the fluid descending the cold inclined wall. This decrease continues until a minimum is reached at the location where the right-counterclockwise rotating eddy meets the middle-clockwise rotating eddy, and the flow is directed downward as a plume toward the opposite wall, creating a region of low temperature gradient and, thereby, a local minimum in heat transfer. Beyond that point an increase in Nu\* is seen to occur until a peak in heat transfer is obtained at the point where the left eddy and the middle eddy, both carrying hot fluid, impinge on the cold wall. Beyond this region, the fluid temperature and the temperature gradient decrease, causing a decrease in

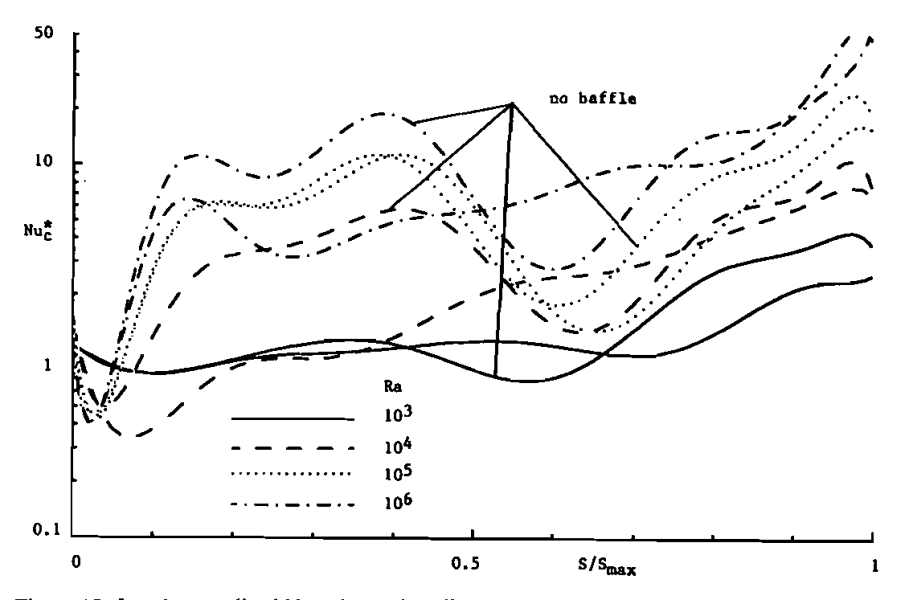


Figure 15. Local normalized Nusselt number distribution along the cold wall for BL = 2W/3 and BH = H/3 (winter).

Nu\* until the cold vertical wall is reached, where the flow re-impinges on the vertical wall, leading to a small peak. While moving down the cold vertical wall, there is a rapid decrease in the convection heat transfer.

In the presence of baffles the Nu distribution is again dictated by the flow field. At Ra = 10<sup>5</sup>, because of the similarity with the flow field obtained in a baffle-free enclosure, the Nu\* distribution is similar except that the Nu\* values are lower. For the other Ra, because the flow field along the cold wall is composed of one counterclockwise rotating eddy, Nu\* decreases from right to left along the cold wall with a small local peak where the flow negotiates the corner with the vertical wall.

Heat transfer results for all cases studied are presented in the form of average normalized Nusselt number values in Table 5. Unlike the summertime boundary condition, convection becomes important at relatively low values of Ra. However, as in the previous case, partitioning the domain decreases the overall heat transfer. For a given baffle height (BH), the decrease in heat transfer increases with increasing distance from the vertical wall (BL) but is relatively unaffected by the baffle height. This is in contrast to the earlier case, where the baffle height played a dominant role in the reductions of heat transfer. The average Nusselt number values, displayed in normalized form in Table 5, are correlated as

$$\overline{\text{Nu}}^* = 1.508(\text{Ra})^{0.229} \left(1 + \frac{\text{BL}}{W}\right)^{-0.198} \left(1 + \frac{\text{BH}}{H}\right)^{0.036}$$
 (26)

with a maximum deviation of less than  $\pm 12.65\%$ . In contrast to Eq. (25), the above equation shows a strong dependence on Ra, a strong inverse dependence on BL/W and a weak dependence on BH/W.

#### **CLOSING REMARKS**

A numerical investigation of natural convection heat transfer in partially divided trapezoidal cavities is performed. The effects of Rayleigh number, baffle height, and baffle location on heat transfer in summer-like (bottom-cooled) and winter-like (bottom-heated) conditions are studied. The following major conclusions are noted.

Table 5. Normalized	l average Nussell	number values	(Nu*)	for winter conditions
---------------------	-------------------	---------------	-------	-----------------------

Ra	BH = 0	BH = H/3		BH = 2H/3		
	BL = 0	BL = W/3	BL = 2W/3	BL = W/3	BL = 2W/3	
103	1.185	1.141	1.047	1.145	1.041	
104	2.317	2.191	1.602	2.004	1.681	
10 <sup>5</sup>	4.055	3.652	3.299	3.144	2.777	
10 <sup>6</sup>	6.360	5.927	4.533	5.276	4.962	

- 1. For the bottom-cooled situation the flow and isotherm patterns in the unheated case are similar to that of a heated vertical enclosure except that stratification effects at the top are important. For the partitioned case, at high Ra, the flow separates in the form of a horizontal shear layer from the symmetry line at a location corresponding to the baffle top. This separated shear layer impinges on the horizontal wall on the far side of the baffle, leading to large local heat transfer rates.
- 2. For the bottom-heated situation, without partitions, a three-cell flow pattern is noted for Ra > 10<sup>4</sup>, with plume-like behavior leading to local peaks in the heat transfer distributions. In the presence of partitions, either a two-cell or a three-cell flow pattern could be obtained, depending on Rayleigh number. These flow patterns have corresponding ramifications on the local heat transfer.
- 3. Convection effects are far more pronounced for bottom-heated situations. The presence of baffles decreases heat transfer for both boundary conditions. For the bottom-cooled (summer-like) conditions, the decrease in the heat transfer due to partitions is strongly influenced by the baffle height, with a taller baffle providing greater reduction in heat transfer. For the bottom-heated (winter-like) configuration the reductions in heat transfer are relatively insensitive to baffle height and depend mostly on baffle location, with lower heat transfer for the baffle located closer to the vertical wall.

#### REFERENCES

- 1. S. Ostrach, Natural Convection in Enclosures, *J. Heat Transfer*, vol. 110, pp. 1175–1190, 1988.
- 2. L. Iyican, Y. Bayazitoglu, and L. Witte, An Analytical Study of Natural Convective Heat Transfer Within a Trapezoidal Enclosure, J. Heat Transfer, vol. 102, pp. 640-647, 1980.
- 3. L. Iyican, L. C. Witte, and Y. Bayazitoglu, An Experimental Study of Natural Convection in Trapezoidal Enclosures, J. Heat Transfer, vol. 102, pp. 648-653, 1980.
- 4. S. W. Lam, R. Gani, and J. G. Symons, Experimental and Numerical Studies of Natural Convection in Trapezoidal Cavities, J. Heat Transfer, vol. 111, pp. 372-377, 1989.
- 5. Y. E. Karyakin, Transient Natural Convection in Prismatic Enlcosures of Arbitrary Cross-Section, J. Heat Mass Transfer, vol. 32, no. 6, pp. 1095-1103, 1989.
- V. A. Akinsete and T. A. Coleman, Heat Transfer by Steady Laminar Free Convection in Triangular Enclosure, Int. J. Heat Mass Transfer, vol. 25, no. 7, pp. 991-998, 1982.
- 7. A. Bejan and D. Poulikakos, Natural Convection in an Attic Shaped Space Filled with Porous Material, *J. Heat Transfer*, vol. 104, pp. 241-247, 1982.
- 8. D. Poulikakos and A. Bejan, The Fluid Dynamics of an Attic Space, *J. Fluid Mech.*, vol. 131, pp. 251-269, 1983.
- 9. D. Poulikakos and A. Bejan, Natural Convection in a Triangular Enclosure, *J. Heat Transfer*, vol. 105, pp. 652-655, 1983.
- 10. Y. E. Karyakin, Y. A. Sokovishin, and O. G. Matynenko, Transient Natural Convection in Triangular Enclsoures, *J. Heat Mass Transfer*, vol. 31, no. 9, pp. 1759-1766, 1988.
- 11. C. M. Rhie and W. L. Chow, Numerical Study of the Turbulent Flow Past an Airfoil with Trailing Edge Separation, AIAA J., vol. 21, pp. 1525-1532, 1983.
- 12. S. V. Patankar, Numerical Heat Transfer and Fluid Flow, Hemisphere, New York, 1980.

- 13. S. Acharya and F. H. Moukalled, Improvements to Incompressible Flow Calculation on a Nonstaggered Curvilinear Grid, *J. Numer. Heat Transfer*, *Part B*, vol. 15, pp. 131–152, 1989.
- 14. W. J. Gordon and C. A. Hall, Construction of Curvilinear Coordinate Systems and Applications to Mesh Generation, J. Numer. Methods Eng., vol. 7, pp. 461-477, 1973.
- 15. W. J. Gordon and L. C. Theil, Transfinite Mappings and Their Applications to Grid Generation, in J. F. Thompson (ed.), *Numerical Grid Generation*, pp. 171-192, North Holland, New York, 1982.
- 16. R. Haber, M. S. Shephard, J. F. Abel, R. H. Gallagher and D. P. Grennberg, A General Two-Dimensional, Graphical Finite Element Pre-Processor Utilizing Discrete Transfinite Mappings, J. Numer. Methods Eng., vol. 17, pp. 1015-1044, 1981.
- E. Zimmerman and S. Acharya, Influence of Aperture Location on Free Convection in Partially Divided Enclosure, J. Thermophys. Heat Transfer, vol. 2, no. 2, pp. 184-186, 1988
- 18. M. W. Nansteel and R. Greif, Natural Convection in Undivided and Partially Divided Rectangular Enclosures, J. Heat Transfer, vol. 103, pp. 623-629, 1984.
- 19. H. Salmun, Convection Patterns in a Triangular Domain, *Int. J. Heat Mass Transfer*, vol. 38, no. 2, pp. 351-362, 1995.